Applied Catalysis B: Environment and Energy 356 (2024) 124222

Contents lists available at ScienceDirect

Applied Catalysis B: Environment and Energy

journal homepage: www.elsevier.com/locate/apcatb

Asymmetric aggregation enables red-light CO_2 reduction with tunable activity and selectivity by intermolecular electronic coupling

Chun Hao [a,1], Yue Sun [a,1], Hu Shi [a,b], Hongxia Zhang [a], Jianghong Zhao [a], Hengquan Yang [a], Pengju Yang [a,*]

[a] School of Chemistry and Chemical Engineering, Shanxi University, Taiyuan 030006, China
[b] Institute of Molecular Science, Shanxi University, Taiyuan 030006, China

ARTICLE INFO

Keywords:
Aggregation
Photocatalysis
Red light
Charge separation
CO_2 photoreduction

ABSTRACT

Photocatalytic CO_2 reduction to value-added chemicals is a promising way to simultaneously mitigate environmental and energy issues. Integrating low-energy red light harvesting, fast charge separation, and robust CO_2 activation in a photosystem is a crucial prerequisite for highly efficient CO_2 photoreduction but remains a huge challenge. Herein, we constructed an aggregated [Ru(2, 2'-bipyridine)$_3$]Cl_2 (denoted as Ru(bpy)$_3Cl_2$) photosystem. Various characterizations combining molecular dynamic simulations and theoretical calculations confirm that the electronic coupling between adjacent Ru(bpy)$_3Cl_2$ molecules can induce orbital hybridization, thus broadening the light absorption edge to the red light region. Meanwhile, the asymmetric aggregation of Ru(bpy)$_3Cl_2$ enables exciton dissociation and charge transfer through a dipole polarization effect. Significantly, this dipole polarization can also upshift the d-orbital of Ni catalytic centers, greatly strengthening the activation of CO_2 and lowering the formation energy barrier of COOH* intermediates. Consequently, the apparent quantum yield (AQY) of aggregates for CO_2-to-CO reduction reaches 4.2% at 610 nm, significantly higher than the AQYs of other reported photosystems at wavelengths $\geq$ 600 nm. More importantly, the catalytic efficiency and selectivity of CO_2 reduction can be rationally tuned by controlling the aggregated degrees of Ru(bpy)$_3Cl_2$. This work highlights the key role of Ru(bpy)$_3Cl_2$ aggregation in prompting red-light harvesting and CO_2 activation, which may help boost CO_2 photoreduction efficiency from a fresh perspective.

1. Introduction

Photocatalytic CO_2 reduction into value-added products is a promising path to address energy and environmental issues [1–3]. In the solar spectrum, visible and near-infrared (NIR) light account for 95% of the solar spectrum [4]. Given solar energy utilization, photocatalysts need to capture the broad spectrum of solar light. Still, most existing photocatalysts are usually active under ultraviolet or narrow visible light and display serious charge recombination [5]. Especially, many organic photocatalysts have poor stability because high-energy ultraviolet and visible light irradiation could cause structural transformation [6]. In principle, low-energy red/NIR-light-responsive photosystems may overcome these issues. However, only a few photocatalysts can drive CO_2 reduction with red or NIR light. For example, Kang and co-workers constructed a CNDs/Cu_2O photocatalytic system, which showed high photocatalytic activities under NIR light irradiation by up-conversion [7]. Xiong and co-workers employed the Au rod as a plasmonic light-harvesting unit and copper-palladium alloy shell as a co-catalyst, achieving CO_2 reduction under full-spectrum light illumination [8]. Xie and co-workers synthesized an ultrathin oxygen-deficient cubic WO_3 layers, realizing IR-driven CO_2 overall splitting by a defect-induced intermediate band [9]. However, these reported systems show moderate photocatalytic activity. This is because most red/NIR-light-response photocatalysts typically exhibit narrow energy gaps, leading to improper band-edge positions for CO_2 reduction [9,10]. Furthermore, most existing photocatalysts have inefficient CO_2 activation owing to the chemical inertness of linear CO_2. Therefore, it is significant to construct a photosystem that possesses red/NIR light harvesting, efficient charge separation, suitable redox potentials, and robust CO_2 activation simultaneously.

The π-conjugated organic molecules are of growing interest in the field of photocatalysis. It has been proven that molecular packing/

* Corresponding author.
E-mail address: yangpengju10@mails.ucas.ac.cn (P. Yang).
[1] These authors contributed equally to this work

https://doi.org/10.1016/j.apcatb.2024.124222
Received 28 February 2024; Received in revised form 10 May 2024; Accepted 20 May 2024
Available online 22 May 2024
0926-3373/© 2024 Elsevier B.V. All rights are reserved, including those for text and data mining, AI training, and similar technologies.

aggregation can control optical properties in organic nanomaterials [11,12]. For instance, our group observed that the aggregates of light-active structures can significantly broaden their light-harvesting regions, thereby improving photocatalytic performance [13,14]. Furthermore, the unique electronic coupling within aggregates facilitates charge localization [15,16]. Especially, the spontaneous symmetry breaking of aggregates can generate large dipole moments, which undoubtedly accelerates charge separation and transfer [17,18]. It should be noted that this dipole polarization effect may also regulate the electronic properties of co-catalysts, in principle, probably expediting the activation of CO_2 molecules. Based on the above analysis, the aggregation of light-harvesting units can broaden the light-harvesting region and promote the separation and transfer of charge carriers [19,20]. Significantly, the aggregation of light harvesting units may consolidate the activation of CO_2 by regulating the electronic properties of co-catalysts. However, to the best of our knowledge, the aggregation-enhanced red-light CO_2 reduction has not been examined, and the link between the aggregation of light harvesting units and CO_2 reduction activity remains unclear.

In this work, as a proof-of-concept demonstration, we chose [Ru(2, 2'-bipyridine)$_3$]Cl_2 (denoted as Ru(bpy)$_3Cl_2$) as a light-harvesting unit and systematically studied the aggregated effect of Ru(bpy)$_3Cl_2$ on the red-light-driven CO_2 reduction performance. The structures, photophysical properties, and CO_2 photoreduction activity of Ru(bpy)$_3Cl_2$ aggregates were analyzed carefully. Results confirm that the electronic coupling between adjacent Ru(bpy)$_3Cl_2$ molecules can induce orbital rearrangement, thus extending the light absorption edge to the red light region. Simultaneously, the spontaneous symmetry breaking of Ru(bpy)$_3Cl_2$ aggregates generates a large dipole moment, which boosts the separation and transfer of charge carriers and prolongs the lifetime of charge carriers. Interestingly, this dipole polarization of Ru(bpy)$_3Cl_2$ aggregates can also upshift the d-orbital of Ni catalytic centers, promoting the activation of CO_2 and lowering the formation energy barrier of COOH* species. As a result, the Ru(bpy)$_3Cl_2$ aggregates exhibit excellent CO_2-to-CO reduction activity under red light irradiation with an apparent quantum yield of 4.2% at 610 nm. More importantly, the efficiency and selectivity of this CO_2 photoreduction system can be tuned by changing the aggregated degrees of Ru(bpy)$_3Cl_2$ molecules.

2. Experimental

2.1. Chemicals

All chemicals were analytical-grade and used without further purification. Acetonitrile (≥99.9%), triethanolamine (≥99.5%), sodium sulfate anhydrous (99.5%), and 2,2-bipyridine (≥99.5%) were purchased from Sinopharm Chemical Reagent Co., Ltd. 2, 2'-Bipyridine nickel dichloride (≥99.9%) and cetyl trimethyl ammonium bromide (≥99.9%) were purchased from Macklin. [Ru(bpy)$_3$]Cl_2·6 H_2O (≥99.0%) was obtained from Alfa Aesar.

2.2. Preparation of droplet-confined Ru(bpy)$_3Cl_2$

Ru(bpy)$_3Cl_2$ with different amounts were respectively dissolved in water/acetonitrile (2 mg/mL for droplet-A, 4 mg/mL for droplet-B, 8 mg/mL for droplet-C). Then, the above Ru(bpy)$_3Cl_2$ solution was injected into 10 mL hexane containing 30 mg cetyl trimethyl ammonium bromide, while ultrasonic treatment was carried out for 5 min under continuous stirring to form uniform droplets (the overall mass of Ru(bpy)$_3Cl_2$ within the above three droplets are controlled to be 8 mg).

2.3. Characterization

UV–vis absorption spectra of all samples were analyzed using a HITACHI UH5700 UV-Vis-NIR spectrophotometer. Photoluminescence (PL) spectra and time-resolved photoluminescence of all samples were measured by a FL spectrophotometer (FLSP920, FLS1000). Confocal laser microscopy images were obtained with a Carl Zeiss LSM880 instrument. Small-angle X-ray scattering (SAXS) experiment was measured on model Xeuss 2.0 instrument from Xenocs, France, the incident beam was Cu Kα radiation (λ = 0.1542 nm). The data was fitted to the model in the SasView software package (version 5.0.6). The error is obtained from the fitting software and does not take into account other sources of error. Cryogenic transmission electron microscopy (Cryo-TEM) was measured by a FEI Talos F200C. The ultrafast femtosecond transient absorption spectra (*fs*-TA) measurement was conducted on a Helios spectrometer using a regeneratively amplified femtosecond Ti: sapphire laser system (Spitfire Pro-F1KXP, Spectra-Physics). Diffuse reflectance infrared Fourier transform spectrum was measured by BRUKER, EQUINOX 55. $^{13}CO_2$ isotope labeling experiment was performed under the same reaction conditions. A gas chromatography-mass spectrometry was used to analyze the generated ^{13}CO. Linear scanning voltammetry experiments were measured by CHI660E C22142. The working electrode was carbon paper, platinum wire as the counter electrode, Ag/AgCl as the reference electrode and the electrolyte solution was an aqueous solution of 0.2 M Na_2SO_4.

2.4. Photocatalytic reaction and apparent quantum yield measurements

Photocatalytic CO_2 reduction reaction was conducted in a closed reaction system. In brief, Ru(bpy)$_3Cl_2$ with different amounts were added to 2 mL of water and 3 mL of acetonitrile. 2, 2'-Bipyridine nickel dichloride (Ni(bpy)Cl_2) and triethanolamine (TEOA) were used as co-catalyst and electron donor, respectively. The air in the reaction bottle was expelled before the reaction, and then the reaction system was filled with CO_2 gas. A 50 W monochromatic LED lamp (610 nm) was used as the light source. The light intensity is controlled to be 110.2 mW·cm^{-2}. The reaction temperature was maintained at room temperature (30 ± 2°C) by using a cooling fan. The rotational speed of the magnet is maintained at 600 rmp. The products during the photocatalytic reaction were quantified by gas chromatography (TCD detector).

The apparent quantum yield (AQY) of CO_2 reduction was measured by using a monochromatic LED lamp as excitation light. The irradiation area was controlled at 0.196 cm^2. The reaction temperature was controlled at room temperature (30 ± 2 °C). The amount of catalyst is 44.8 mg. The rotational speed of the magnet is maintained at 600 rmp. The light intensity of 610 nm was 26.48 mW·cm^{-2} (ILT 950 spectroradiometer).

AQY=Ne/Np*100%=2M NAhc/SPtλ*100%

Where M is the amount of CO (mol), NA is Avogadro constant (6.02×10^{23} mol^{-1}), h is Planck constant (6.626×10^{-34} J • s), c is light speed (3×10^{8} m/s), S is irradiation area (cm^2), P is light intensity (W/cm^2), t is reaction time (s), λ is the wavelength of light irradiation (m).

2.5. Computational details

Classical molecular dynamic (MD) simulations were performed to investigate the structures of Ru(bpy)$_3Cl_2$ in the GROMACS (version 2021.7) simulation package. All of the initial structures were optimized at B3LYP level in Gaussian 09 software. The simulated parameters of Ru(bpy)$_3Cl_2$ were obtained using UFF force filed [21], which has confirmed the accuracy in pieces of literature [22]. During MD simulation, the Particle-mesh Ewald was selected for long-range electrostatics. The cutoff was set at 1.0 nm, and the time step was set at 1 fs. In detail, for pure acetonitrile (ACN) and acetonitrile/cyclohexane (CYH) environments containing the same number of Ru(bpy)$_3Cl_2$ molecules at the size of a = 5.0 nm, b = 5.0 nm, c = 5.0 nm, α = β = γ =90°. Therefore, the 300 ns MD simulations were performed for each system. After equilibration checking, only the final 100 ns converged trajectories were used for further analysis.

All calculations were performed by Gaussian 09 software. The B3LYP functional and mixed basis set of SDD were used to calculate the metal atoms, and the nonmetal atoms were used for geometry optimization of the molecule using 6–31 G* [23,24]. The convergence accuracy of the SCF reaches the default convergence standard. Subsequently, harmonic frequency analysis calculations at the same level were carried out to indicate the absence of imaginary frequencies at the standing point. To obtain more accurate energy, single-point calculation was performed using the higher basis set, where 6–311 G* was used for nonmetal atoms and SDD for metal atoms in a mixture of water and acetonitrile solvents, using the SMD solvent model [25]. The Gibbs free energy was then corrected to the refining energy at 298.15 K and 1 atm. In this study, we discuss the reaction mechanism in terms of the corrected Gibbs free energy given under the corresponding compounds.

Moreover, we calculated electron-hole distribution, excited states, electron density difference, and Mulliken charge populations of the molecules. The geometrical configuration, highest occupied molecular orbital (HOMO)-lowest unoccupied molecular orbital (LUMO) energy gap, excited state orbital distribution, the electrostatic potential at the molecular surface, and dipole moments of $Ru(bpy)_3Cl_2$ have also been visualized by using Multiwfn 3.8 [26] and VMD 1.9.3 [27] software.

3. Results and discussion

3.1. Structural and characterization of $Ru(bpy)_3Cl_2$ aggregates

Fig. 1**a-b** display the UV–vis absorption spectra of $Ru(bpy)_3Cl_2$ with different concentrations. The $Ru(bpy)_3Cl_2$ monomer shows a characteristic peak at 450 nm [28,29]. With the increase of $Ru(bpy)_3Cl_2$ concentrations, the characteristic peak at 450 nm is noticeably red-shifted and the light absorption intensity from 500 to 700 nm can be enhanced significantly [30,31]. This result indicates the formation of $Ru(bpy)_3Cl_2$ aggregates, which is further supported by the calculated bandgaps result of $Ru(bpy)_3Cl_2$ aggregates (Figure S1) [32,33]. To further investigate the formation of $Ru(bpy)_3Cl_2$ aggregates, we analyzed the photoluminescence (PL) spectra of $Ru(bpy)_3Cl_2$ with

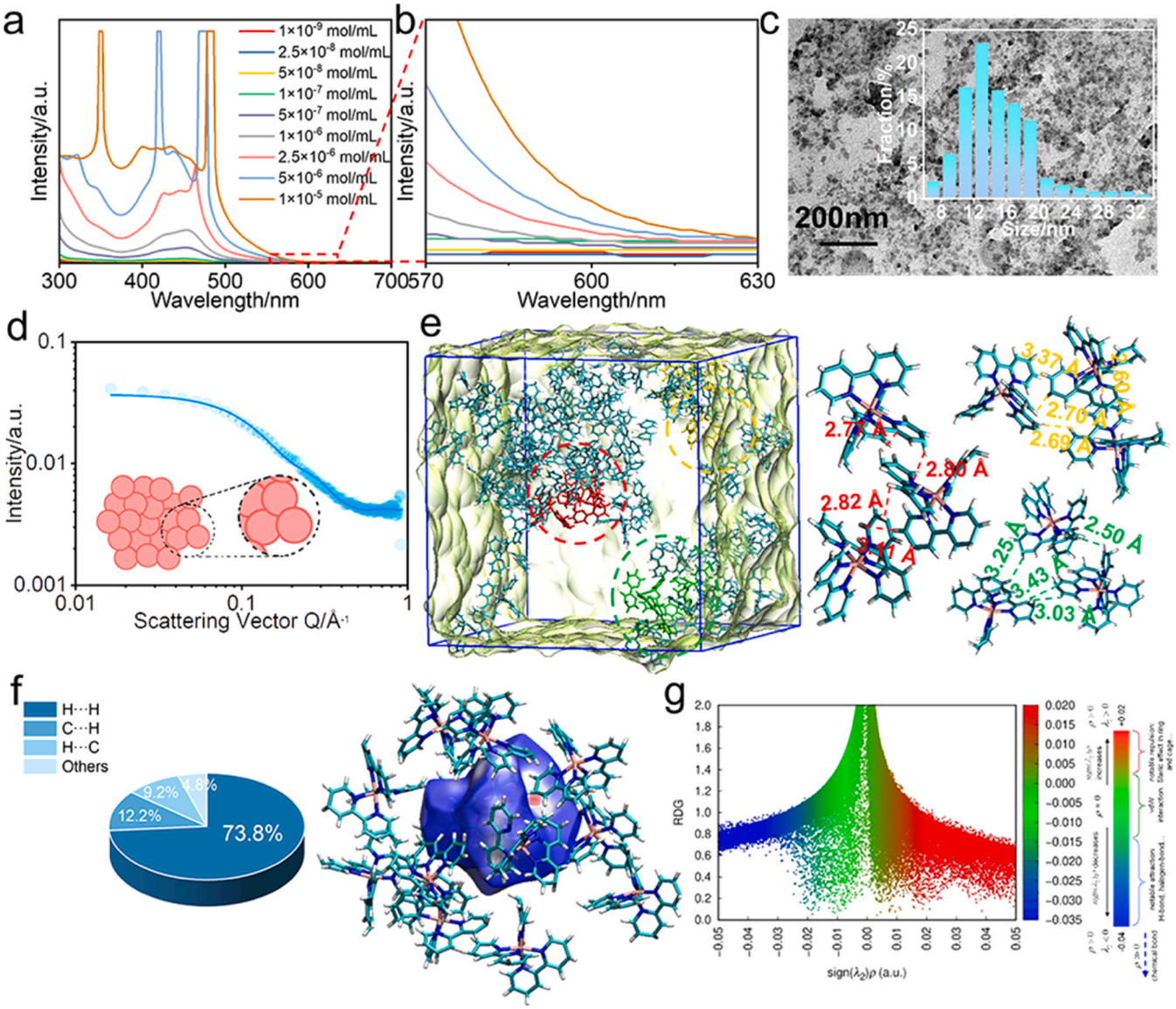

Fig. 1. (a-b) UV–vis absorption spectra of $Ru(bpy)_3Cl_2$ with different concentrations, (c) Cryo-TEM image of $Ru(bpy)_3Cl_2$ aggregates, (d) SAXS data of $Ru(bpy)_3Cl_2$ aggregates, (e) The structures of $Ru(bpy)_3Cl_2$ aggregates by MD simulation, (f) Hirschfeld surface analysis (mapped over d_{norm}), and proportions of intermolecular C···H, H···H, H···C, and other interactions to the total intermolecular interactions based on MD simulation, and (g) The function of reduced density gradient and sign $(\lambda_2)\rho$ scatter spectra for $Ru(bpy)_3Cl_2$ aggregates based on our MD simulation.

different concentrations (Figure S2). It is obvious that the PL emission band is red-shifted with increasing the concentrations of $Ru(bpy)_3Cl_2$. This red-shift behavior of PL emission also reflects the formation of aggregates. The formation of $Ru(bpy)_3Cl_2$ aggregates was imaged using cryogenic transmission electron microscopy (Cryo-TEM) to capture the solution-state morphology and size. As shown in Fig. 1**c**, the $Ru(bpy)_3Cl_2$ aggregates display sphere-like morphology with a narrow size distribution. The small-angle X-ray scattering (SAXS) curve was further employed to determine the structures of $Ru(bpy)_3Cl_2$ aggregates (Fig. 1**d**). The fitting data indicates the existence of sphere-like nanostructures [34,35]. The vanishing of the linear Guinier region can be attributed to aggregation in the sample (Figure S3) [35–37], agreeing with the Cryo-TEM measurement.

To further analyze the microstructures of $Ru(bpy)_3Cl_2$ aggregates, a molecular dynamic (MD) simulation was performed (Fig. 1**e**). The $Ru(bpy)_3Cl_2$-$Ru(bpy)_3Cl_2$ contact map authorizes that the $Ru(bpy)_3Cl_2$ molecules tend to interact with adjacent $Ru(bpy)_3Cl_2$ molecules (Figure S4). The distances of neighboring $Ru(bpy)_3Cl_2$ molecules are ranged from 2.5 to 3.59 Å (Figure S5). Interestingly, the distances and angles of adjacent $Ru(bpy)_3Cl_2$ molecules are different, suggesting the asymmetric feature of $Ru(bpy)_3Cl_2$ aggregates. Therefore, Hirshfeld surface analysis based on MD simulation was performed to quantitatively estimate the intermolecular interactions (Fig. 1**f** and **S6**) [38,39]. The weak intermolecular C···H, H···H, and H···C interactions account for more than 95% of total intermolecular interactions, indicating that weak non-covalent interactions mainly contribute to the aggregation of $Ru(bpy)_3Cl_2$. Reduced density gradient (RDG) scattering spectrum also ratifies the presence of weak intermolecular interactions in the $Ru(bpy)_3Cl_2$ aggregates (Fig. 1**g**), consistent with the findings of Hirshfeld surface analysis [40,41].

Considering the red-shifted light absorption of $Ru(bpy)_3Cl_2$ aggregates, the $Ru(bpy)_3Cl_2$-$Ru(bpy)_3Cl_2$ orbital interactions analysis is necessary to understand the electronic coupling between adjacent $Ru(bpy)_3Cl_2$ molecules [42,43]. As revealed in Fig. 2, the LUMO orbital of the trimer mainly originates from the 131st orbital of Fragment 1 (95%), with a decrease in energy of 5.87 eV. The HOMO orbital mainly originates from the 130th orbital of Fragment 3 (94%), with an increase in energy of 5.11 eV. The LUMO+1 and HOMO-1 orbitals are respectively derived from the 134th orbital of Fragment 1 (64%) and the 130th orbital of Fragment 2 (75%). These results confirm the existence of strong electronic coupling between adjacent $Ru(bpy)_3Cl_2$ molecules, which rearranges their molecular orbitals (MOs), in agreement with the orbital analysis of the dimer and tetramer (Figures S7 and S8) [44]. The above results suggest intermolecular weak interactions can induce orbital rearrangements and hybridization of $Ru(bpy)_3Cl_2$ molecules, thus generating new light-harvesting properties. It should be noted that weak non-covalent interactions are not unusual in organic molecules but have been overlooked in the past. The above discovery will deepen the understanding of intermolecular weak forces and offer a promising route to regulate the physicochemical properties, especially the optical properties of photocatalytic materials from a fresh perspective.

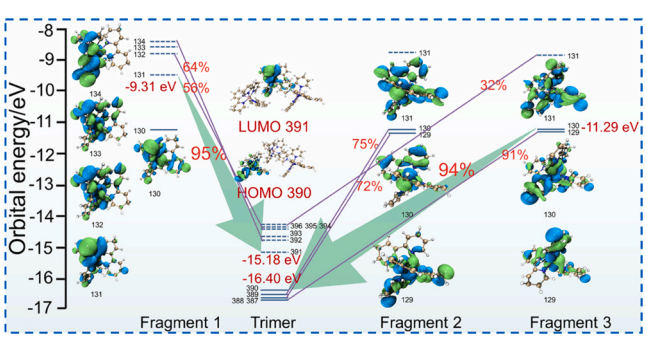

Fig. 2. Orbital interaction diagram for $Ru(bpy)_3Cl_2$ aggregates. The vertical axis shows MO energies in eV. Blue solid and dashed bars correspond to occupied and unoccupied MOs, respectively. The MOs are plotted as isosurface graphs with isovalue of 0.02 a.u.

In principle, the asymmetric feature of $Ru(bpy)_3Cl_2$ aggregates could induce the generation of large dipole moments, which boosts the separation of photogenerated charge carriers. Therefore, we statistically analyzed the dipole moments of $Ru(bpy)_3Cl_2$ aggregates with different aggregated degrees based on MD simulation. The dipole moment of $Ru(bpy)_3Cl_2$ monomer is calculated to be 0.509 Debye (denoted as 0.509 D) (Figure S9). Significantly, the dipole moments of aggregates increase with increasing the aggregated degrees of $Ru(bpy)_3Cl_2$ (Figures S9-**12**). The large dipole moments of the $Ru(bpy)_3Cl_2$ aggregates can be primarily ascribed to structural symmetry breaking [45]. Interestingly, we also observed the dynamical behaviors of $Ru(bpy)_3Cl_2$ aggregates due to the weak interactions between adjacent $Ru(bpy)_3Cl_2$ molecules. Randomly selected snapshot images of $Ru(bpy)_3Cl_2$ aggregates recorded at 94, 95, 96, 97, 98, and 99 ns display different local structures (Fig. 3) and electron density distributions (Figure S13), reflecting their dynamical nature. This dynamic behavior was found to stabilize the asymmetric structures of $Ru(bpy)_3Cl_2$ aggregates. It has been widely accepted that large dipole moments can result in a strong built-in electric field, which will certainly accelerate exciton dissociation and charge transfer [46,47]. To confirm this deduction, we calculated the exciton binding energies of $Ru(bpy)_3Cl_2$ aggregates by using the Multiwfn program. Impressively, the exciton binding energy sharply decreases from 4.767 eV for $Ru(bpy)_3Cl_2$ monomer to 0.730 eV for tetramer aggregates, consistent with the results of electron-hole distributions (Figure S14). The decreased exciton binding energy reflects that the aggregation of $Ru(bpy)_3Cl_2$ can expedite exciton dissociation into free electrons and holes, which increases the probability of electrons and holes participating in redox reactions [48,49].

Furthermore, the steady-state PL emission intensity of $Ru(bpy)_3Cl_2$ aggregates is lower than that of $Ru(bpy)_3Cl_2$ monomer, which suggests an enhanced charge separation of $Ru(bpy)_3Cl_2$ aggregates (Figure S15). Also, we observed that the PL lifetime of $Ru(bpy)_3Cl_2$ aggregates can be significantly prolonged (Figure S15), signifying an enhanced chance for photogenerated electrons participating in CO_2 reduction, in agreement with the steady-state PL emission results. To deeply explore the aggregated effect of $Ru(bpy)_3Cl_2$ on charge separation and transfer dynamics, we estimated the femtosecond transient absorption (*fs*-TA) spectra of $Ru(bpy)_3Cl_2$ monomer and aggregates, as illustrated in Figs. S16 and 4**b**. *fs*-TA demonstrates the absorption spectra versus time and wavelength. The $Ru(bpy)_3Cl_2$ monomer displays a weak absorption (excited state absorption, ESA) [50,51]. The fitting lifetime at 615 nm is 3.86 ns (Table S2). Whereas, the $Ru(bpy)_3Cl_2$ aggregates exhibit a strong ESA signal. Compared to the $Ru(bpy)_3Cl_2$ monomer, the $Ru(bpy)_3Cl_2$ aggregates exhibit different dynamic behavior, which reflects the unique interactions within aggregates. The fitting lifetime at 615 nm is 28.5 ns for $Ru(bpy)_3Cl_2$ aggregates, which is longer than that for $Ru(bpy)_3Cl_2$ monomer. Significantly, a new transient absorption band at 755 nm was witnessed, which belongs to the charge transfer (CT) state [50,51]. The fitting lifetime of CT state is 18.7 ns (Fig. 4**c** and Table S2). It is widely recognized that the CT state can easily overcome the Coulombic attraction of excitons to form free charges on the time scale of picoseconds. The formation of CT state reflects an effective exciton dissociation and charge transfer dynamics of $Ru(bpy)_3Cl_2$ aggregates, consistent with the above results of DFT predictions, steady-state PL, and time-resolved PL spectra [52–55]. Moreover, we have also estimated the CO_2 absorption ability of the aggregates (Figure S17). The aggregates show obvious CO_2 absorption capability, providing the possibility for CO_2 reduction.

3.2. Photocatalytic activity test

Intrigued by the enhanced light harvesting and the effective charge separation of $Ru(bpy)_3Cl_2$ aggregates, we investigated their

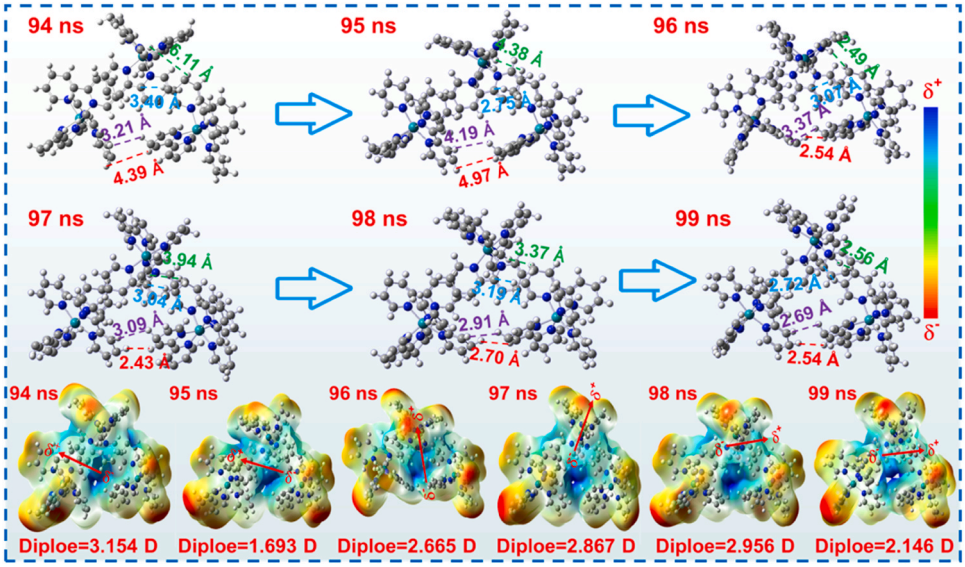

Fig. 3. Dynamic properties of trimer aggregates in MD snapshot with related dipole moments and electrostatic potential distributions.

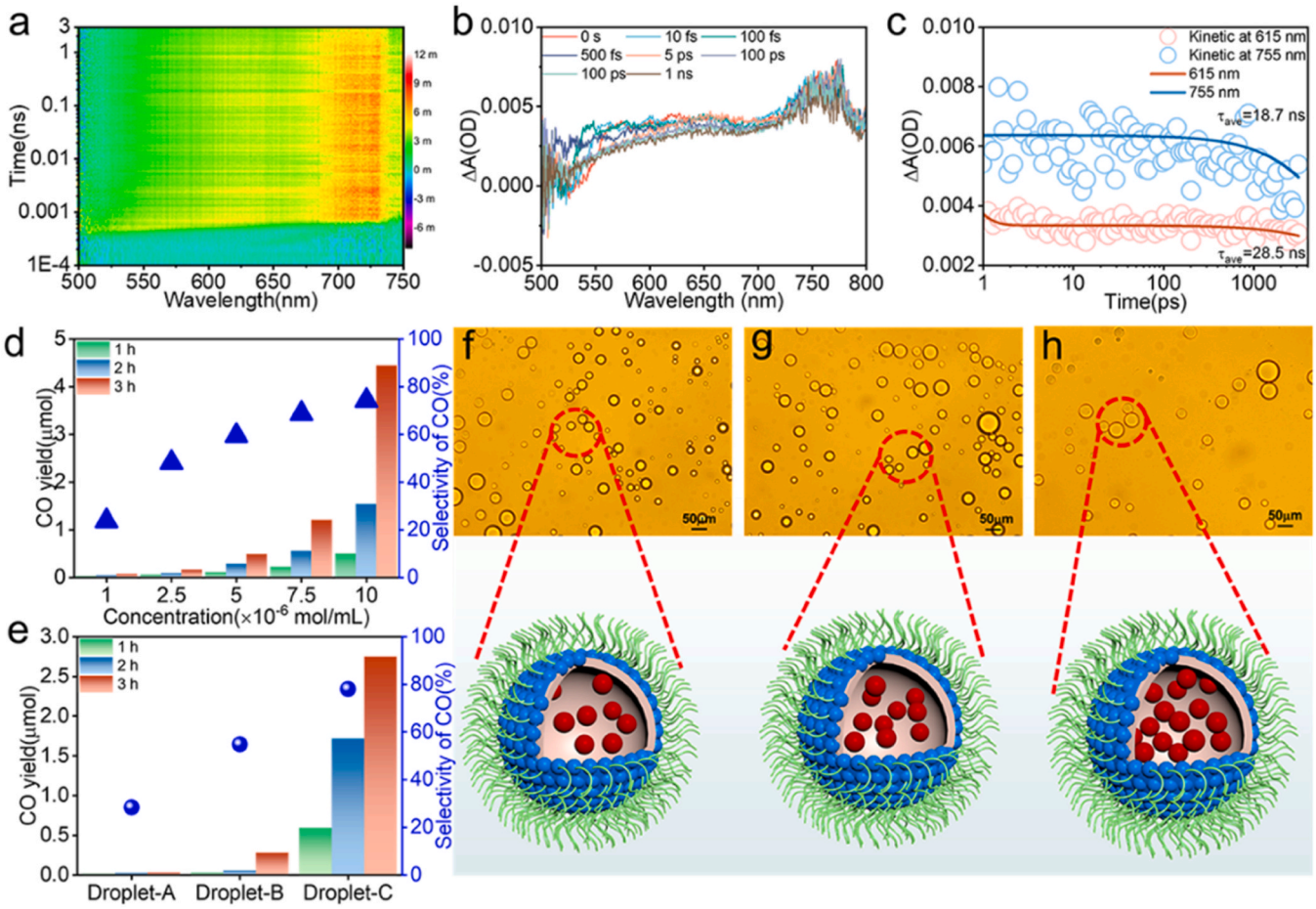

Fig. 4. (a) 2D transient absorption surface plot of $Ru(bpy)_3Cl_2$ aggregates, (b) *fs*-TA spectra of the $Ru(bpy)_3Cl_2$ aggregates, (c) Decay kinetics probed at 615 and 755 nm, (d) Photocatalytic CO_2 reduction activity of $Ru(bpy)_3Cl_2$ with different $Ru(bpy)_3Cl_2$ concentrations, (e) Photocatalytic CO_2 reduction performances of droplet-confined $Ru(bpy)_3Cl_2$ under 610 nm light irradiation and (f-h) Optical microscope images of droplet-A, droplet-B, and droplet-C, and schematic illustration of the droplet-confined $Ru(bpy)_3Cl_2$ aggregates.

photocatalytic CO_2 reduction performance under red light (610 nm) irradiation. As shown in Fig. 4**d**, when the concentration of $Ru(bpy)_3Cl_2$ is relatively low (monomer), only trace amounts of CO are detected (3 h reaction, 0.0734 μmol CO, CO selectivity of 23.7%, H_2 as a byproduct). Impressively, as the concentrations of $Ru(bpy)_3Cl_2$ increase, the CO yield significantly increases (3 h reaction, 13.2 μmol CO, CO selectivity

of 80.6%). The generated CO was verified from CO_2 reduction through a ^{13}C isotope experiment (Figure S18). Furthermore, the aggregates also display good durability for CO_2 reduction (Figure S19). In addition, some blank experiments were carried out under the same reaction conditions. In the absence of $Ru(bpy)_3Cl_2$ aggregates, without light irradiation, without CO_2 and TEOA, no product was detected (Figure S20). These results indicated that the $Ru(bpy)_3Cl_2$ aggregates and light were essential for CO_2 reduction reaction.

Furthermore, we normalized CO production rates based on the amount of $Ru(bpy)_3Cl_2$. Obviously, with increasing the amounts of $Ru(bpy)_3Cl_2$, CO production rates harshly increase (Figure S21), which indicates that the aggregation of $Ru(bpy)_3Cl_2$ has a major influence on the CO_2 reduction efficiency, and also reveals the existence of strong synergistic effect within $Ru(bpy)_3Cl_2$ aggregates. To further explore the impact of $Ru(bpy)_3Cl_2$ aggregation on the photocatalytic performance toward CO_2 reduction, three water-in-oil droplets containing different concentrations of $Ru(bpy)_3Cl_2$ were prepared. The concentrations of $Ru(bpy)_3Cl_2$ in droplets A, B, and C were 2, 4, and 8 mg/mL, respectively. The total mass of $Ru(bpy)_3Cl_2$ confined in the three droplets is controlled to be 8 mg. Optical microscope images of droplets A, B, and C are presented in Fig. 4**f-g**. It was found that the rates of CO production are positively correlated with the aggregated degrees of $Ru(bpy)_3Cl_2$ (Fig. 4**e**). Since the total mass of $Ru(bpy)_3Cl_2$ in the three droplets is the same, the high photocatalytic activity of $Ru(bpy)_3Cl_2$ aggregates confined in droplet C can be safely ascribed to the high aggregated degree of $Ru(bpy)_3Cl_2$. Interestingly, we have also observed that the selectivity of CO increases from 23.7% to 74.2% with increasing the aggregated degrees of $Ru(bpy)_3Cl_2$ (Fig. 4**d**), consistent with droplet-confined $Ru(bpy)_3Cl_2$ (Fig. 4**e**). Therefore, the above results undoubtedly confirm that the aggregation of $Ru(bpy)_3Cl_2$ plays a key role in determining the photocatalytic performance of CO_2 reduction.

3.3. Electronic property analysis

MD simulation and DFT calculations confirm that the $Ru(bpy)_3Cl_2$ aggregates exhibit asymmetric structures and large dipole moments. In principle, the dipole polarization effect probably influences the electronic properties of $Ni(bpy)Cl_2$ co-catalyst and thus regulates the activity and selectivity toward CO_2 reduction reaction. To check this, the charge density difference of $Ni(bpy)Cl_2/Ru(bpy)_3Cl_2$ was calculated (Fig. 5**a-b**). Compared with the $Ni(bpy)Cl_2/Ru(bpy)_3Cl_2$ monomer, the $Ni(bpy)Cl_2/Ru(bpy)_3Cl_2$ aggregates display different charge distributions [56–58]. A Mulliken charge population analysis suggests that the charge transfer amount from the $Ru(bpy)_3Cl_2$ aggregates to the Ni catalytic centers is

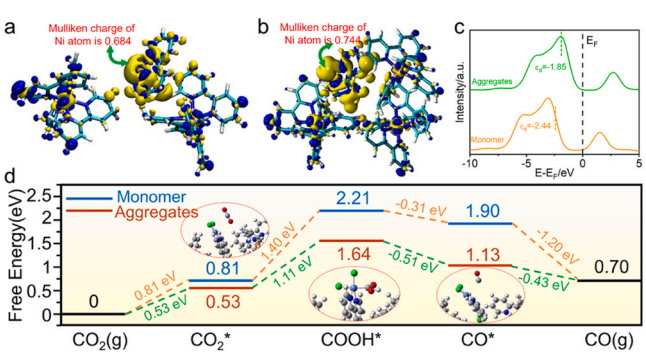

Fig. 5. (a) Charge density difference of $Ni(bpy)Cl_2/Ru(bpy)_3Cl_2$ monomer (isovalue = 0.001 a.u., yellow and blue areas represent charge accumulation and depletion, respectively), (b) Charge density difference of $Ni(bpy)Cl_2/Ru(bpy)_3Cl_2$ aggregates (isovalue = 0.001 a.u., yellow and blue areas represent charge accumulation and depletion, respectively), (c) The pDOS of $Ni(bpy)Cl_2/Ru(bpy)_3Cl_2$ monomer and $Ni(bpy)Cl_2/Ru(bpy)_3Cl_2$ aggregates, and (d) Calculated free energy diagrams for CO_2 reduction over $Ni(bpy)Cl_2/Ru(bpy)_3Cl_2$ monomer and $Ni(bpy)Cl_2/Ru(bpy)_3Cl_2$ aggregates.

higher than that from the $Ru(bpy)_3Cl_2$ monomer to the Ni catalytic center [59,60]. Furthermore, the projected density of states (pDOS) suggests that the d-orbital center of Ni within the $Ni(bpy)Cl_2/Ru(bpy)_3Cl_2$ aggregates up-shifts to the Fermi energy (E_F) level (Fig. 5**c**) [61–63]. The up-shift of the d-orbital center for Ni probably derives from the strong charge redistribution caused by the dipole polarization effect of aggregated systems. According to the d-band center theory, the higher d-orbital center indicates a stronger binding energy between the Ni catalytic centers and CO_2, which reflects the strengthened activation ability of CO_2 over the Ni catalytic centers, thus promoting the activity and selectivity of CO_2-to-CO reduction [64,65]. Furthermore, the linear sweep voltammetry result also indicates that the aggregation of $Ru(bpy)_3Cl_2$ could indeed promote the catalytic ability of the Ni catalytic center, consistent with the above results and analysis (Figure S22).

In-situ diffuse reflectance infrared Fourier transform spectroscopy (DRIFTS) was performed to monitor the reduction processes of CO_2 over the $Ni(bpy)Cl_2/Ru(bpy)_3Cl_2$ aggregates (Figure S23). The signal at 2355 cm^{-1} corresponds to the symmetric stretching vibration modes of CO_2 [66]. Significantly, the intermediate species of COOH* for CO_2-to-CO (peaks at 1521, 1543 and 1558 cm^{-1}) were witnessed [67]. Furthermore, we calculated the reaction Gibbs free energy change (ΔG) of CO_2-to-CO reduction on the $Ni(bpy)Cl_2/Ru(bpy)_3Cl_2$ aggregates [68, 69]. Optimized geometric structures of various states over the $Ni(bpy)Cl_2/Ru(bpy)_3Cl_2$ aggregates along the reaction pathway are presented in Figure S24. Compared with the $Ni(bpy)Cl_2/Ru(bpy)_3Cl_2$ monomer, the $Ni(bpy)Cl_2/Ru(bpy)_3Cl_2$ aggregates have a lower ΔG for the formation of COOH* species, which is the rate-determining step of CO_2 reduction to CO (Fig. 5**d**) [70–72]. This result reflects that the aggregation of $Ru(bpy)_3Cl_2$ can lower the energy barrier for the formation of COOH* intermediates. It is widely believed that increased electron density of co-catalysts can boost CO_2 activation because the electrons in co-catalysts could occupy the anti-bonding orbital of CO_2 and force the linear CO_2 to bend. Therefore, the lowered formation energy of COOH* intermediates can be primarily attributed to the high electron density around Ni catalytic centers induced by the dipole polarization effect of $Ru(bpy)_3Cl_2$ aggregates, consistent with the results of Mulliken charge calculation and d-orbital center analysis. To our knowledge, this is the first observation that asymmetric aggregation of $Ru(bpy)_3Cl_2$ light-harvesting unit can modulate the electron structures of Ni co-catalyst and thus boost CO_2 reduction, which will open a new avenue to manipulate the selectivity and activity of CO_2 reduction reaction.

To further improve the activity of CO_2 photoreduction, cyclohexane/acetonitrile mixed solvent was employed to modulate the local interaction within $Ru(bpy)_3Cl_2$ aggregates. MD simulation (Fig. 6**a**) and $Ru(bpy)_3Cl_2$--$Ru(bpy)_3Cl_2$ contact map (Fig. 6**b** and **S25**) suggest that the introduction of cyclohexane has a slight influence on the aggregated process of $Ru(bpy)_3Cl_2$. Interestingly, Hirshfeld surface analysis proposes that cyclohexane influences the intermolecular interactions within $Ru(bpy)_3Cl_2$ aggregates (Fig. 6**c** and **S26**) [38,39]. Meanwhile, we calculated the interaction force between $Ru(bpy)_3Cl_2$ and acetonitrile/cyclohexane (Figure S27). The result suggests that the relatively weak pulling effect of cyclohexane can help to promote the $Ru(bpy)_3Cl_2$-$Ru(bpy)_3Cl_2$ intermolecular interactions. Furthermore, we randomly analyzed the local structures of 30 regions based on MD simulation. The statistical analysis reveals that the introduction of cyclohexane can indeed increase the intermolecular interaction strength of neighboring $Ru(bpy)_3Cl_2$ molecules (Figures S28-**30**). Fig. 6**d** displays the UV–vis absorption spectra of $Ru(bpy)_3Cl_2$ aggregates after the addition of cyclohexane. Obviously, the optical absorption intensity is improved substantially, signifying a decreased bandgap energy [10,30]. To further check this, we calculated the bandgap values for $Ru(bpy)_3Cl_2$ aggregates with different intermolecular distances. It was found that a closer intermolecular distance of $Ru(bpy)_3Cl_2$ will result in a smaller bandgap (Figure S31), agreeing with the UV–vis absorption result. Besides, the PL lifetime of $Ru(bpy)_3Cl_2$ aggregates increases when cyclohexane is introduced (Fig. 6**e** and Table S1), signifying an increased

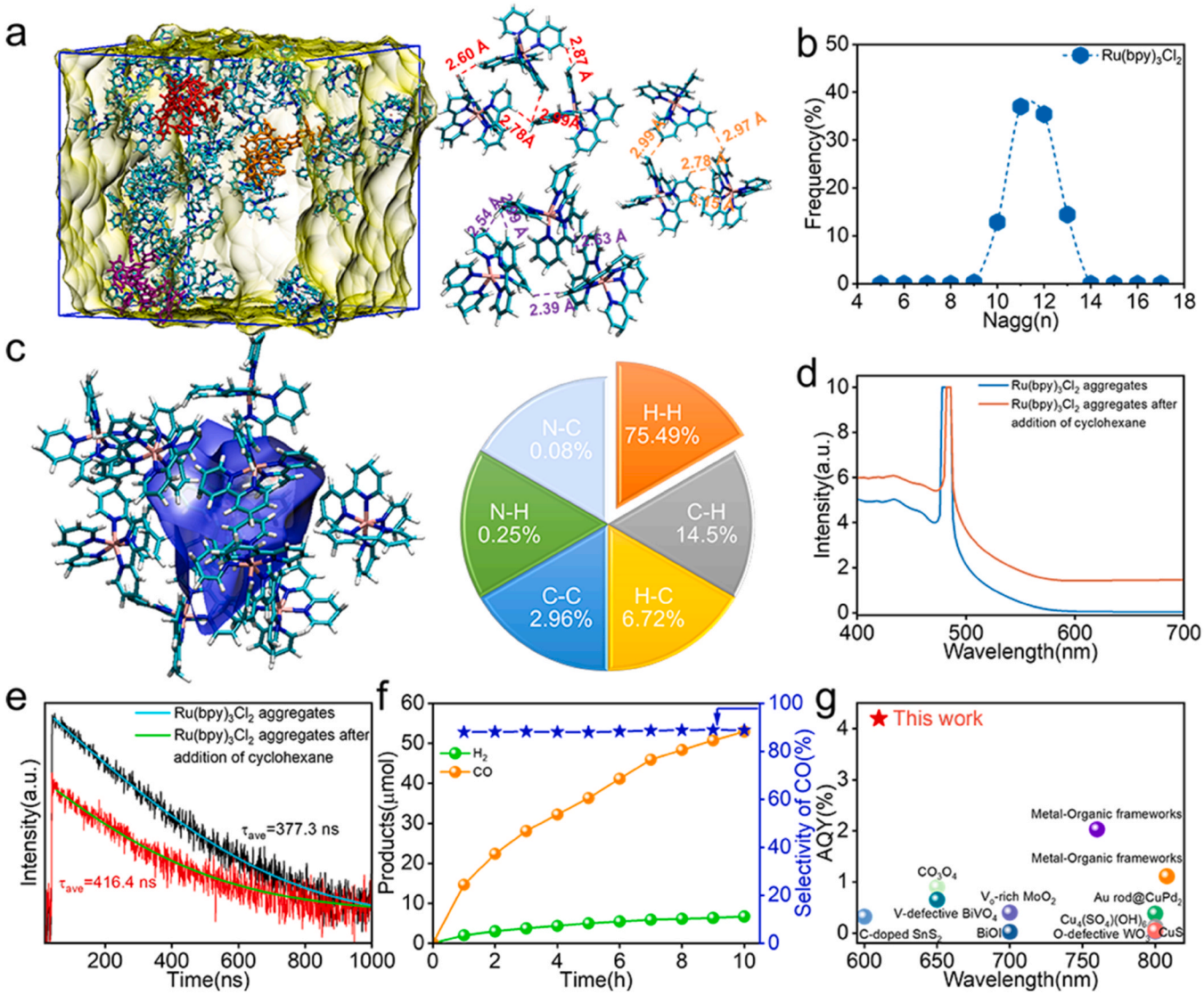

Fig. 6. (a) Structures of $Ru(bpy)_3Cl_2$ aggregates in acetonitrile/cyclohexane by MD simulation, (b) The number distribution of $Ru(bpy)_3Cl_2$ aggregates based on MD simulation, (c) Hirschfeld surface analysis (mapped over d_{norm}), and proportions of intermolecular C···H, H···H, H···C, and other interactions to the total intermolecular interactions based on MD simulated structures, (d) UV–vis absorption spectra of $Ru(bpy)_3Cl_2$ aggregates after the addition of cyclohexane, (e) Time-resolved PL spectra of $Ru(bpy)_3Cl_2$ aggregates with and without adding cyclohexane, (f) Photocatalytic stability of $Ru(bpy)_3Cl_2$ aggregates after adding cyclohexane, and (g) Comparison of CO_2 photoreduction performance with state-of-the-art photocatalysts under red/NIR light irradiation (see Table S3 for details).

chance for photogenerated electrons participating in CO_2 reduction. As anticipated, the $Ru(bpy)_3Cl_2$ aggregates show a 2.6-fold enhancement in CO production with a selectivity of 88% (Fig. 6**f** and **S32**). Meanwhile, the $Ru(bpy)_3Cl_2$ aggregates exhibit admirable stability (Fig. 6**f**), well supported by the Cryo-TEM analysis of $Ru(bpy)_3Cl_2$ aggregates before and after the reaction (Figure S33) [73,74]. Impressively, the apparent quantum yield (AQY) of $Ru(bpy)_3Cl_2$ aggregates for CO production was estimated to be as high as 4.2% at 610 nm, superior to those of the reported red/NIR-light-driven CO_2 reduction systems (Fig. 6**g** and Table S3).

Based on the above analysis, a proposed mechanism of red-light-driven CO_2 reduction over the $Ru(bpy)_3Cl_2$ aggregates is presented (Fig. 7). Firstly, the $Ru(bpy)_3Cl_2$ aggregates capture red light by the unique electronic coupling between adjacent $Ru(bpy)_3Cl_2$ molecules and generate electron-hole pairs. Secondly, the dipole polarization induced by the asymmetric aggregation of $Ru(bpy)_3Cl_2$ promotes long-range charge delocalization, exciton dissociation, and formation of CT state, accelerating the separation and transfer of photogenerated charge carriers. Importantly, the dipole polarization of $Ru(bpy)_3Cl_2$ aggregates

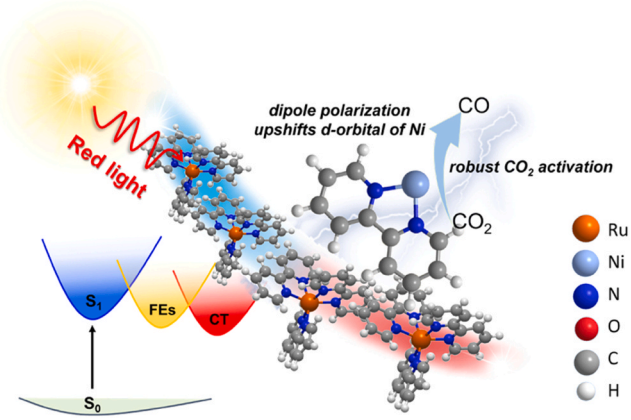

Fig. 7. A proposed mechanism for CO_2 reduction over $Ru(bpy)_3Cl_2$ aggregates under red light.

is favorable for charge redistribution and hence up-shifts the d-orbital center of Ni co-catalysts, consolidating the activation of CO_2. This photosystem reported here integrates strong red-light harvesting, fast charge separation, and robust CO_2 activation, which synergistically improves the performance toward CO_2 reduction.

4. Conclusion

In this work, we systematically investigated the aggregated effect of $Ru(bpy)_3Cl_2$ on the red-light-driven CO_2 reduction performance. The structures, photophysical properties, and CO_2 photoreduction activity of $Ru(bpy)_3Cl_2$ aggregates were analyzed by various characterizations. Results authorize that the electronic coupling between adjacent Ru $(bpy)_3Cl_2$ molecules induces orbital rearrangements and hybridization, thereby expanding the light absorption edge to the red light region. Meanwhile, the spontaneous symmetry breaking of $Ru(bpy)_3Cl_2$ aggregates accelerates charge separation and transfer, while prolonging the lifetime of charge carriers. Significantly, the symmetry-breaking-induced dipole polarization was found to up-shift the d-orbital center of Ni co-catalysts to the Fermi energy level, which effectively facilitates CO_2 activation and lowers the energy barrier for COOH* intermediates formation. This aggregated photosystem integrates low-energy strong red-light harvesting, fast charge separation, suitable redox potentials, and robust CO_2 activation, which can serve as an unprecedented platform for efficient CO_2 photoreduction. This work deepens the understanding of intermolecular weak forces for tuning the physicochemical properties of aggregates and may offer a way from a new view to control the catalytic activity and selectivity of photocatalytic systems.

CRediT authorship contribution statement

Hongxia Zhang: Funding acquisition, Formal analysis, Data curation. **Hu Shi:** Software, Project administration, Methodology. **Yue Sun:** Methodology, Investigation. **Chun Hao:** Investigation, Data curation. **Pengju Yang:** Writing – review & editing, Writing – original draft, Visualization, Validation, Supervision, Resources, Funding acquisition, Formal analysis, Conceptualization. **Hengquan Yang:** Project administration, Methodology, Investigation. **Jianghong Zhao:** Project administration, Methodology, Investigation.

Declaration of Competing Interest

We declare that we have no financial and personal relationships with other people or organizations that can inappropriately influence our work.

Data availability

No data was used for the research described in the article.

Acknowledgment

This work was financially supported by the National Natural Science Foundation of China (Grant No. 22372094), the Natural Science Foundation of Shanxi Province (Grant No.20210302123461), the Central Guidance Local Science and Technology Development in Shanxi Province Project (YDZJSX2021A001), the Science and Technology Major Project of the Shanxi Science and Technology Department (Grant Nos. 201903D121003 and 20181102019).

Notes

The authors declare no competing financial interest.

Appendix A. Supporting information

Supplementary data associated with this article can be found in the online version at doi:10.1016/j.apcatb.2024.124222.

References

[1] Z. Jiang, X. Xu, Y. Ma, H.S. Cho, D. Ding, C. Wang, J. Wu, P. Oleynikov, M. Jia, J. Cheng, Y. Zhou, O. Terasaki, T. Peng, L. Zan, H. Deng, Filling metal-organic framework mesopores with TiO_2 for CO_2 photoreduction, Nature 586 (2020) 549–554.
[2] S.N. Habisreutinger, L. Schmidt-Mende, J.K. Stolarczyk, Photocatalytic reduction of CO_2 on TiO_2 and other semiconductors, Angew. Chem. Int. Ed. 52 (2013) 7372–7408.
[3] J.W. Fu, K.X. Jiang, X.Q. Qiu, J.G. Yu, M. Liu, Product selectivity of photocatalytic CO_2 reduction reactions, Mater. Today 32 (2020) 222–243.
[4] L. Liang, X. Li, J. Zhang, P. Ling, Y. Sun, C. Wang, Q. Zhang, Y. Pan, Q. Xu, J. Zhu, Y. Luo, Y. Xie, Efficient infrared light induced CO_2 reduction with nearly 100% CO selectivity enabled by metallic CoN porous atomic layers, Nano Energy 69 (2020) 104421.
[5] W. Ma, J. Sun, S. Yao, Y. Wang, G. Chen, G. Fan, Y. Li, Synergistic interplay of dual-active-sites on metallic Ni-MOFs loaded with Pt for thermal-photocatalytic conversion of atmospheric CO_2 under infrared light irradiation, Angew. Chem. Int. Ed. 62 (2023) e202313784.
[6] Z. Zhang, X. Chen, H. Zhang, W. Liu, W. Zhu, Y. Zhu, A highly crystalline perylene imide polymer with the robust built-in electric field for efficient photocatalytic water oxidation, Adv. Mater. 32 (2020) e1907746.
[7] H. Li, R. Liu, Y. Liu, H. Huang, H. Yu, H. Ming, S. Lian, S.-T. Lee, Z. Kang, Carbon quantum dots/Cu_2O composites with protruding nanostructures and their highly efficient (near) infrared photocatalytic behavior, J. Mater. Chem. 22 (2012) 17470.
[8] C. Hu, X. Chen, J. Low, Y.W. Yang, H. Li, D. Wu, S. Chen, J. Jin, H. Li, H. Ju, C. H. Wang, Z. Lu, R. Long, L. Song, Y. Xiong, Near-infrared-featured broadband CO_2 reduction with water to hydrocarbons by surface plasmon, Nat. Commun. 14 (2023) 221.
[9] L. Liang, X. Li, Y. Sun, Y. Tan, X. Jiao, H. Ju, Z. Qi, J. Zhu, Y. Xie, Infrared light-driven CO_2 overall splitting at room temperature, Joule 2 (2018) 1004–1016.
[10] X. Jiao, K. Zheng, Z. Hu, Y. Sun, Y. Xie, Broad-spectral-response photocatalysts for CO_2 reduction, ACS Cent. Sci. 6 (2020) 653–660.
[11] K. Rybicka-Jasinska, W. Shan, K. Zawada, K.M. Kadish, D. Gryko, Porphyrins as photoredox catalysts: experimental and theoretical studies, J. Am. Chem. Soc. 138 (2016) 15451–15458.
[12] W. Auwarter, D. Ecija, F. Klappenberger, J.V. Barth, Porphyrins at interfaces, Nat. Chem. 7 (2015) 105–120.
[13] P. Yang, Q. Zhang, Y. Zhang, H. Zhang, J. Zhao, H. Shi, L. Liang, Y. Huang, Z. Zheng, H. Yang, Aggregation triggers red/near-infrared light hydrogen production of organic dyes with high efficiency, ACS Catal. 13 (2023) 3723–3734.
[14] Q. Zhang, Y. Zhang, H. Shi, H. Zhang, J. Zhao, Z. Zheng, H. Yang, P. Yang, Dynamic aggregation of carbon dots self-stabilizes symmetry breaking for exceptional hydrogen production with near-infrared light, Aggregate (2023) e424.
[15] T. He, Y. Zhang, H. Zhang, J. Zhao, H. Shi, H. Yang, P. Yang, Aggregation-induced structural symmetry breaking promotes charge separation for efficient photocatalytic hydrogen production, ChemSusChem 16 (2023) e202300500.
[16] S. Kang, T. Kim, Y. Hong, F. Wurthner, D. Kim, Charge-delocalized state and coherent vibrational dynamics in rigid PBI H-aggregates, J. Am. Chem. Soc. 143 (2021) 9825–9833.
[17] C. Cai, K. Liu, L. Zhang, F. Li, Y. Tan, P. Li, Y. Wang, M. Wang, Z. Feng, D. Motta Meira, W. Qu, A. Stefancu, W. Li, H. Li, J. Fu, H. Wang, D. Zhang, E. Cortes, M. Liu, Atomically local electric field induced interface water reorientation for alkaline hydrogen evolution reaction, Angew. Chem. Int. Ed. 62 (2023) e202300873.
[18] W. Du, H. Shi, H. Zhang, J. Zhao, H. Yang, P. Yang, Controlled asymmetric aggregation advances n→π* electronic transition and charge separation for enhanced photocatalytic hydrogen synthesis, J. Catal. 432 (2024) 115453.
[19] J. Sung, P. Kim, B. Fimmel, F. Wurthner, D. Kim, Direct observation of ultrafast coherent exciton dynamics in helical π-stacks of self-assembled perylene bisimides, Nat. Commun. 6 (2015) 8646.
[20] F.S. Freyria, J.M. Cordero, J.R. Caram, S. Doria, A. Dodin, Y. Chen, A.P. Willard, M. G. Bawendi, Near-infrared quantum dot emission enhanced by stabilized self-assembled J-aggregate antennas, Nano Lett. 17 (2017) 7665–7674.
[21] A.K. Rappe, C.J. Casewit, K.S. Colwell, W.A. Goddard, W.M. Skiff, UFF, a full periodic-table force field for molecular mechanics and molecular dynamics simulations, J. Am. Chem. Soc. 114 (1992) 10024–10035.
[22] D.E. McCoy, T. Feo, T.A. Harvey, R.O. Prum, Structural absorption by barbule microstructures of super black bird of paradise feathers, Nat. Commun. 9 (2018) 1.
[23] M.M. Francl, W.J. Pietro, W.J. Hehre, J.S. Binkley, M.S. Gordon, D.J. DeFrees, J. A. Pople, Self-consistent molecular orbital methods. XXIII. A polarization-type basis set for second-row elements, J. Chem. Phys. 77 (1982) 3654–3665.
[24] D. Andrae, U. Haussermann, M. Dolg, H. Stoll, H. Preuss, Engery-adjustedab initio pseudopotentials for the second and third row transition-elements, Theor. Chim. Acta 77 (1990) 123–141.
[25] A.V. Marenich, C.J. Cramer, D.G. Truhlar, Universal solvation model based on solute electron density and on a continuum model of the solvent defined by the bulk dielectric constant and atomic surface tensions, J. Phys. Chem. B 113 (2009) 6378–6396.

[26] T. Lu, F. Chen, Multiwfn: a multifunctional wavefunction analyzer, J. Comput. Chem. 33 (2012) 580–592.
[27] W. Humphrey, A. Dalke, K. Schulten, VMD: Visual molecular dynamics, J. Mol. Graph. Model. 14 (1996) 33–38.
[28] A.C. Bhasikuttan, M. Suzuki, S. Nakashima, T. Okada, Ultrafast fluorescence detection in tris(2,2′-bipyridine)ruthenium(II) complex in solution: relaxation dynamics involving higher excited states, J. Am. Chem. Soc. 124 (2002) 8398–8405.
[29] P. Kumar, C. Joshi, A.K. Srivastava, P. Gupta, R. Boukherroub, S.L. Jain, Visible light assisted photocatalytic [3+2] azide-alkyne "Click" reaction for the synthesis of 1,4-substituted 1,2,3-triazoles using a novel bimetallic Ru-Mn complex, ACS Sustain. Chem. Eng. 4 (2015) 69–75.
[30] H. Zhang, Z. Zhao, A.T. Turley, L. Wang, P.R. McGonigal, Y. Tu, Y. Li, Z. Wang, R.T. K. Kwok, J.W.Y. Lam, B.Z. Tang, Aggregate science: from structures to properties, Adv. Mater. 32 (2020) e2001457.
[31] J. Sturala, M.K. Etherington, A.N. Bismillah, H.F. Higginbotham, W. Trewby, J. A. Aguilar, E.H.C. Bromley, A.J. Avestro, A.P. Monkman, P.R. McGonigal, Excited-state aromatic interactions in the aggregation-induced emission of molecular rotors, J. Am. Chem. Soc. 139 (2017) 17882–17889.
[32] Y. Feng, T. Bai, H. Yan, F. Ding, L. Bai, W. Feng, High fluorescence quantum yield based on the through-space conjugation of hyperbranched polysiloxane, Macromolecules 52 (2019) 3075–3082.
[33] Z. Zhang, J. Wang, D. Liu, W. Luo, M. Zhang, W. Jiang, Y. Zhu, Highly efficient organic photocatalyst with full visible light spectrum through π-π stacking of TCNQ-PTCDI, ACS Appl. Mater. Interfaces 8 (2016) 30225–30231.
[34] D. McDowall, B.J. Greeves, R. Clowes, K. McAulay, A.M. Fuentes-Caparrós, L. Thomson, N. Khunti, N. Cowieson, M.C. Nolan, M. Wallace, A.I. Cooper, E. R. Draper, A.J. Cowan, D.J. Adams, Controlling photocatalytic activity by self-assembly-tuning perylene bisimide photocatalysts for the hydrogen evolution reaction, Adv. Energy Mater. 10 (2020) 2002469.
[35] T. Kamarainen, K. Kadota, J.Y. Tse, H. Uchiyama, T. Oguchi, H. Arima-Osonoi, Y. Tozuka, Tuning the phytoglycogen size and aggregate structure with solvent quality: influence of water-ethanol mixtures revealed by X-ray and light scattering techniques, Biomacromolecules 24 (2023) 225–237.
[36] T.D. Grant, J.R. Luft, L.G. Carter, T. Matsui, T.M. Weiss, A. Martel, E.H. Snell, The accurate assessment of small-angle X-ray scattering data, Acta Crystallogr. D. 71 (2015) 45–56.
[37] A.H. Larsen, J.S. Pedersen, L. Arleth, Assessment of structure factors for analysis of small-angle scattering data from desired or undesired aggregates, J. Appl. Cryst. 53 (2020) 991–1005.
[38] A.V. Parwani, Expression of glypican 3 in ovarian and extragonadal germ cell tumors, Am. J. Clin. Pathol. 2009 (2009) 93–95.
[39] J. Zhang, P. Alam, S. Zhang, H. Shen, L. Hu, H.H.Y. Sung, I.D. Williams, J. Sun, J. W.Y. Lam, H. Zhang, B.Z. Tang, Secondary through-space interactions facilitated single-molecule white-light emission from clusteroluminogens, Nat. Commun. 13 (2022) 3492.
[40] Y. Kumar, A. Sudhaik, K. Sharma, Sonu, P. Raizada, A. Aslam Parwaz Khan, V.-H. Nguyen, T. Ahamad, P. Singh, A.M. Asiri, Construction of magnetically separable novel arrow down dual S-scheme $ZnIn_2S_4$/BiOCl/$FeVO_4$ heterojunction for improved photocatalytic activity, J. Photochem. Photobiol. A 435 (2023) 114326.
[41] V. Dutta, S. Sonu, P. Raizada, V.K. Thakur, T. Ahamad, S. Thakur, P. Kumar Verma, H.H.P. Quang, V.H. Nguyen, P. Singh, Prism-like integrated Bi_2WO_6 with Ag-$CuBi_2O_4$ on carbon nanotubes (CNTs) as an efficient and robust S-scheme interfacial charge transfer photocatalyst for the removal of organic pollutants from wastewater, Environ. Sci. Pollut. Res. 30 (2023) 124530–124545.
[42] X. Wang, Z. Liu, X. Yan, T. Lu, W. Zheng, W. Xiong, Bonding character, electron delocalization, and aromaticity of cyclo[18]carbon (C_{18}) precursors, C_{18}-$(CO)_n$ (n=6, 4, and 2): Focusing on the effect of carbonyl (-CO) groups, Chem. Eur. J. 28 (2022) e202103815.
[43] S. Manzetti, T. Lu, H. Behzadi, M.D. Estrafili, H.-L. Thi Le, H. Vach, Intriguing properties of unusual silicon nanocrystals, RSC Adv. 5 (2015) 78192–78208.
[44] P. Yang, Y. Zhang, H. Zhang, J. Zhao, Z. Wei, H. Shi, Z. Zheng, Y. Huang, H. Yang, Hydrogen-bonded aggregates featuring n→π* electronic transition for efficient visible-light-responsive photocatalysis, ACS Catal. 12 (2022) 6276–6284.
[45] G. Ran, J. Zeb, Y. Song, P.A. Denis, U. Ghani, W. Zhang, Photoinduced symmetry breaking-charge separation in the aggregated state of perylene diimide: effect of hydrophobicity, J. Phys. Chem. C. 126 (2022) 3872–3880.
[46] H. Lin, J. Wang, J. Zhao, Y. Zhuang, B. Liu, Y. Zhu, H. Jia, K. Wu, J. Shen, X. Fu, X. Zhang, J. Long, Molecular dipole-induced photoredox catalysis for hydrogen evolution over self-assembled naphthalimide nanoribbons, Angew. Chem. Int. Ed. 61 (2022) e202117645.
[47] Y. Guo, Q. Zhou, J. Nan, W. Shi, F. Cui, Y. Zhu, Perylenetetracarboxylic acid nanosheets with internal electric fields and anisotropic charge migration for photocatalytic hydrogen evolution, Nat. Commun. 13 (2022) 2067.
[48] J. Xiao, Z. Xiao, J. Hu, X. Gao, M. Asim, L. Pan, C. Shi, X. Zhang, J.-J. Zou, Rational design of alkynyl-based linear donor-π-acceptor conjugated polymers with accelerated exciton dissociation for photocatalysis, Macromolecules 55 (2022) 5412–5421.
[49] F. Meng, J. Wang, M. Chen, Z. Wang, G. Bai, X. Lan, Extending the π-conjugated system in conjugated microporous polymers to modulate excitonic effects for metal-free selective CO_2 photoreduction to CH_4, ACS Catal. 13 (2023) 12142–12152.
[50] C.M. Wolff, P.D. Frischmann, M. Schulze, B.J. Bohn, R. Wein, P. Livadas, M. T. Carlson, F. Jäckel, J. Feldmann, F. Würthner, J.K. Stolarczyk, All-in-one visible-light-driven water splitting by combining nanoparticulate and molecular co-catalysts on CdS nanorods, Nat. Energy 3 (2018) 862–869.
[51] C. Bie, B. Zhu, L. Wang, H. Yu, C. Jiang, T. Chen, J. Yu, A bifunctional CdS/MoO_2/MoS_2 catalyst enhances photocatalytic H_2 evolution and pyruvic acid synthesis, Angew. Chem. Int. Ed. 61 (2022) e202212045.
[52] B. Cai, H. Song, A. Brnovic, M.V. Pavliuk, L. Hammarstrom, H. Tian, Promoted charge separation and long-lived charge-separated state in porphyrin-viologen dyad nanoparticles, J. Am. Chem. Soc. 145 (2023) 18687–18692.
[53] Y. Hu, F. Zhan, Q. Wang, Y. Sun, C. Yu, X. Zhao, H. Wang, R. Long, G. Zhang, C. Gao, W. Zhang, J. Jiang, Y. Tao, Y. Xiong, Tracking mechanistic pathway of photocatalytic CO_2 reaction at Ni sites using operando, time-resolved spectroscopy, J. Am. Chem. Soc. 142 (2020) 5618–5626.
[54] K. Wu, H. Zhu, Z. Liu, W. Rodriguez-Cordoba, T. Lian, Ultrafast charge separation and long-lived charge separated state in photocatalytic CdS-Pt nanorod heterostructures, J. Am. Chem. Soc. 134 (2012) 10337–10340.
[55] Sonu, V. Dutta, A. Sudhaik, A.A.P. Khan, T. Ahamad, P. Raizada, S. Thakur, A. M. Asiri, P. Singh, GCN/$CuFe_2O_4$/SiO_2 photocatalyst for photo-Fenton assisted degradation of organic dyes, Mater. Res. Bull. 164 (2023) 112238.
[56] W. Lyu, Y. Liu, J. Zhou, D. Chen, X. Zhao, R. Fang, F. Wang, Y. Li, Modulating the reaction configuration by breaking the structural symmetry of active sites for efficient photocatalytic reduction of low-concentration CO_2, Angew. Chem. Int. Ed. 62 (2023) e202310733.
[57] J.M. Wang, Q.Y. Zhu, J.H. Lee, T.G. Woo, Y.X. Zhang, W.D. Jang, T.K. Kim, Asymmetric gradient orbital interaction of hetero-diatomic active sites for promoting C-C coupling, Nat. Commun. 14 (2023) 3808.
[58] Z. Yang, H. Zhang, J. Zhao, H. Shi, Y. Liu, H. Yang, P. Yang, Light-induced synthesis of oxygen-vacancy-functionalized $Ni(OH)_2$ nanosheets for highly selective CO_2 reduction, ChemSusChem 15 (2022) e202200260.
[59] L.U. Tian, C. Fei-Wu, Comparison of computational methods for atomic charges, Acta Phys. -Chim. Sin. 28 (2012) 1–18.
[60] J. Xu, S. Zhang, H. Liu, S. Liu, Y. Yuan, Y. Meng, M. Wang, C. Shen, Q. Peng, J. Chen, X. Wang, L. Song, K. Li, W. Chen, Breaking local charge symmetry of iron single atoms for efficient electrocatalytic nitrate reduction to ammonia, Angew. Chem. Int. Ed. 62 (2023) e202308044.
[61] X. Ding, Y. Jin, H. Wang, D. Qi, Molecular modification of planar four-coordinated cobalt active site for the electrochemical reduction of carbon dioxide: a density functional theory study, Inorg. Chem. Front. 10 (2023) 7054–7063.
[62] Y. Zhou, R. Duan, H. Li, M. Zhao, C. Ding, C. Li, Boosting electrocatalytic nitrate reduction to ammonia via promoting water dissociation, ACS Catal. 13 (2023) 10846–10854.
[63] G. Dong, X. Huang, Y. Bi, Anchoring black phosphorus quantum dots on Fe-doped $W_{18}O_{49}$ nanowires for efficient photocatalytic nitrogen fixation, Angew. Chem. Int. Ed. 61 (2022) e202204271.
[64] J.R. Huang, X.F. Qiu, Z.H. Zhao, H.L. Zhu, Y.C. Liu, W. Shi, P.Q. Liao, X.M. Chen, Single-product faradaic efficiency for electrocatalytic of CO_2 to CO at current density larger than 1.2 A cm^{-2} in neutral aqueous solution by a single-atom nanozyme, Angew. Chem. Int. Ed. 61 (2022) e202210985.
[65] H. Li, M. Xia, X. Wang, B. Chong, H. Ou, B. Lin, G. Yang, Efficient reduction of CO_2 to C_2 hydrocarbons by tandem nonthermal plasma and photocatalysis, Appl. Catal. B: Environ. 342 (2024) 123423.
[66] P. Yang, L. Shang, J. Zhao, M. Zhang, H. Shi, H. Zhang, H. Yang, Selectively constructing nitrogen vacancy in carbon nitrides for efficient syngas production with visible light, Appl. Catal. B: Environ. 297 (2021) 120496.
[67] P. Yang, H. Zhuzhang, R. Wang, W. Lin, X. Wang, Selectively constructing nitrogen vacancy in carbon nitrides for efficient syngas production with visible light, Appl. Catal. B: Environ. 297 (2021) 75–78.
[68] C. Wang, X. Chen, H. Pan, D. Qi, J. Jiang, Towards developing efficient aminopyridine-based electrochemical catalysts for CO_2 reduction. A density functional theory study, J. Catal. 373 (2019) 75–80.
[69] X. Chen, C. Wang, D. Qi, X. Xing, A theoretical approach for homogeneous CO_2 reduction by Ni(cyclam): substituents with intra-molecular hydrogen transfer, Inorg. Chem. Front. 9 (2022) 2691–2696.
[70] J. Wang, K. Sun, D. Wang, X. Niu, Z. Lin, S. Wang, W. Yang, J. Huang, H.-L. Jiang, Precise regulation of the coordination environment of single Co(II) sites in a metal-organic framework for boosting CO_2 photoreduction, ACS Catal. 13 (2023) 8760–8769.
[71] Z. Zeng, L.Y. Gan, H. Bin Yang, X. Su, J. Gao, W. Liu, H. Matsumoto, J. Gong, J. Zhang, W. Cai, Z. Zhang, Y. Yan, B. Liu, P. Chen, Orbital coupling of hetero-diatomic nickel-iron site for bifunctional electrocatalysis of CO_2 reduction and oxygen evolution, Nat. Commun. 12 (2021) 4088.
[72] Q. Zhang, P. Yang, H. Zhang, J. Zhao, H. Shi, Y. Huang, H. Yang, Oxygen vacancies in Co_3O_4 promote CO_2 photoreduction, Appl. Catal. B: Environ. 300 (2022) 120729.
[73] H. Song, J. Yu, Z. Tang, B. Yang, S. Lu, Halogen-doped carbon dots on amorphous cobalt phosphide as robust electrocatalysts for overall water splitting, Adv. Energy Mater. 12 (2022) 2102573.
[74] H. Song, X. Yong, G.I.N. Waterhouse, J. Yu, H. Wang, J. Cai, Z. Tang, B. Yang, J. Chang, S. Lu, RuO_2-CeO_2 lattice matching strategy enables robust water oxidation electrocatalysis in acidic media via two distinct oxygen evolution mechanisms, ACS Catal. 14 (2024) 3298–3307.